Applied Catalysis B: Environment and Energy 347 (2024) 123808

Contents lists available at ScienceDirect

Applied Catalysis B: Environment and Energy

journal homepage: www.elsevier.com/locate/apcatb

Simultaneously uranium reduction and organics degradation by a drivingpowers enhanced photocatalytic fuel cell based on a UiO-66-NH_2 derived zirconia/N-dopped porous carbon cathode

Qingsong Zhang [a,*], Qimou Deng [a], Yaoyao Zhang [a], Yang Xiao [b,*], Chunlei Zhang [a], Haiyi Gong [a], Qingming Zeng [a], Qingyan Zhang [a], Qingyi Zeng [a,*]

[a] School of Resource & Environment and Safety Engineering, University of South China, Hengyang 421001, China
[b] School of Nuclear Science and Technology, University of South China, Hengyang 421001, China

ARTICLE INFO

Keywords:
Uranium
Photocatalytic fuel cell
Zirconia
N-doped porous carbon
Organic degradation

ABSTRACT

Unavoidable organics in uranium wastewater or contaminated waters derive great challenges to traditional uranium removal techniques. Here, a drivingpower enhanced photocatalytic fuel cell (DEPFC) is designed by using a carbon felt (CF)-based UiO-66-NH_2 derived zirconia (ZrO_2)/N-doped porous carbon (ZrON-C/CF) cathode and a monolithic photoanode, composing of a front FTO glass-based $BiVO_4$ film and a rearmounted Si photovoltaic cell, for effectively oxidizing organics and simultaneously reducing UO_2^{2+} from complex wastewater under sunlight illumination. The water contact angle measurements demonstrate that ZrO_2 can improve the hydrophilia of cathode thus increases the contact between UO_2^{2+} and cathode. The density functional theory indicates that N-doping can enhance the electronegativity of cathode and increases UO_2^{2+} adsorption. Meanwhile, the enhanced UO_2^{2+} reduction facilitates the charge separation in $BiVO_4$ film, therefore enhancing the organic oxidation. Consequently, under AM 1.5 illumination, the designed DEPFC can remove almost 100% of UO_2^{2+} and simultaneous degrade 99% organics within 40 min

1. Introduction

Nuclear energy has been regarded as an ideal solution to the global energy crisis, providing high energy density and without greenhouse gas emissions [1,2]. Uranium, which is considered as the main material for sustainably energized nuclear reactors, is an indispensable nuclear energy resource not only in the moment but also in the future [3,4]. However, during the utilization of uranium, large amounts of uranium containing wastewaters are generated, which seriously threatens the safety of humans and ecological environment due to their natural radioactivity and chemical toxicity [5–7]. In addition, uranium contaminated water often coexists with other organic matters because of the widely use of chemical products and illegal discharge of industrial pollutants [8–10]. The organics bring great challenges to the removal of uranium by traditional methods including adsorption [9], chemical precipitation [11], ion exchange [12] and membrane separation [13], because their competition of adsorption sites, inhibition of ion exchange, contamination of membrane, etc [8,14]. Additionally, the coordination between uranyl ions (UO_2^{2+}, typically stable and soluable uranium species in water) and organic matters makes the situation even worse [15]. To eliminate the effect of organics and achieve highly efficient uranium removal, it is fascinating to search an efficient technology that can simultaneously degrade organic matters and remove UO_2^{2+}.

Photocatalytic fuel cell (PFC), which integrates the photocatalysis, photoelectric conversion and organic fuel cell, has attracted broad attentions in recent years [16–19]. The entire system is composed of a photoanode and cathode and worked under light irradiation. When photoanode is excited by photon with sufficient energy, electrons and holes can be generated. The holes retain in the photoanode and participate in the oxidation of organic contaminants, while the electrons are driven by the different Fermi levels between photoanode and cathode, and can migrate to the cathode by external circuit for electricity generation [20]. In addition to electricity generation, electrons transferred to the cathode can be also employed to reduce the metal ions. For example, Sun et al. designed a multifunctional PFC with TiO_2 as photoanode and Ag@Fe_2O_3 as cathode to degrade organic dyes and simultaneously reduce Cr(VI) [21]; Lam et al. used MoO_3/ZnO/Zn as photoanode and Pt/C as cathode to fabricate PFC for oxidation of phenol

* Corresponding authors.
E-mail addresses: qszhang@usc.edu.cn (Q. Zhang), xiaoyang950529@163.com (Y. Xiao), qszhang@usc.edu.cn (Q. Zhang), qingyizeng@usc.edu.cn (Q. Zeng).

https://doi.org/10.1016/j.apcatb.2024.123808
Received 27 October 2023; Received in revised form 28 December 2023; Accepted 1 February 2024
Available online 3 February 2024

and reduction of Cu^{2+} simultaneously [22]. Therefore, it is reasonable to propose that the degradation of organic matters and reduction of U(VI) can be synchronously realized by PFC, while it is rarely reported yet. For treating uranium containing wastewater, the design of cathode with outstanding electron conductivity and high UO_2^{2+} reduction activity would be of great importance to achieve highly efficient treatment performance.

Recently, carbon materials are widely used in photocatalytic and electrocatalytic field due to their high catalytic activity and electrical conductivity [23,24]. Moreover, elements doping or nanomaterials introduction are believed to further reinforce the chemical and electronic properties of carbon materials to enhance catalytic activity [25]. For example, the N-doping can improve the electronegativity of carbon and also increase the varieties and numbers of nitrogen-containing functional group, thus enhancing the selective adsorption ability of cathode to positively charged compounds in solution [26–28]. In addition, the doping of N can also promote the electron transfer by breaking the inertia of the carbon structure [29]. The incorporation of hygroscopic nanofillers, such as ZrO_2 can effectively improve the water uptake of carbon materials [30]. Moreover, the metal-N bonds can act as the electrons transmission channel in metal and N concomitant carbon materials, thus decreasing the electron transport resistance [31]. Therefore, metal oxide and none-metal co-doped carbon materials would be ideal candidates as PFC cathode for the reduction of UO_2^{2+}. However, the development of this kind of cathode materials for uranium reduction in PFC is still not reported. Furthermore, in a conventional PFC, the driving force is only offered by the different Fermi energy levels between photoanode and cathode, which is incompetent (i.e., <0.8 V) to efficiently facilitate electrons migration, leading to a poor activity of reduction reaction [32].

Herein, we propose a creative drivingpower enhanced PFC (DEPFC) with an improved driving force and a highly-active ZrO_2/N-codoped carbon cathode (ZrON-C/CF) for efficient UO_2^{2+} reduction and simultaneous organic pollutants oxidation only using sunlight. In the DEPFC, the photoanode is composed of a FTO-based $BiVO_4$ film and a back silicon photovoltaic cell (PC). The front $BiVO_4$ film adsorbs the short wavelength light to produce electrons and holes, and the back PC adsorbs the transmission light with long wavelength to generate much higher interior potential than conventional PFC. The ZrON-C/CF cathode is prepared by carbonizing a carbon felt (CF)-supported UiO-66-NH_2, in which ZrO_2 could increasing the hygroscopicity of carbon material and increases the contact between UO_2^{2+} and cathode. N-doping could heighten the electronegativity and increase the varieties of nitrogen-containing functional groups, thus improving the adsorption capacity of ZrON-C/CF cathode to UO_2^{2+}. The formation of Zr-N bonds could reduce the electron transport resistance due to its electron transmission bridge action. In addition, UiO-66-NH_2 derived carbon materials possess both characteristics of MOFs, large specific surface area, porous structure, regular morphology, highly dispersed ZrO_2 clusters, and characteristics of carbon-based materials, high conductivity, and chemical durability in acid or alkali environment. Benefit from the above advantages, the proposed DEPFC shows excellent performance for UO_2^{2+} removal and simultaneous organic degradation. This work proposes a new method for efficient treatment of complex uranium-organic co-existing radioactive wastewater/polluted water, and provides new insights in designing highly active uranium reduction cathode materials.

2. Experimental section

2.1. Chemicals

Zirconium chloride ($ZrCl_4$), 2-aminoterephthalic acid (BDC-NH_2), terephthalic acid (BDC), N,N-dimethylformamide (DMF, 99%), hydrochloric acid (HCl), sodium hydroxide (NaOH), ethanol, tetracycline hydrochloride and other reagent were purchased from Shanghai Aladdin Biochemical Technology Co.,Ltd., China. $UO_2(NO_3)_2{\cdot}6\ H_2O$ was purchased from Macklin Biochemical Co., Ltd (Shanghai, China). All these reagents were used without further purification.

2.2. Preparation of $BiVO_4$ film

The preparation of $BiVO_4$ film used spin-coating method. Before the spin-coating process, the bismuth-containing solution was obtained by adding 2.43 g $Bi(NO_3)_3{\bullet}5\ H_2O$ into 100 mL deionized water containing 0.2 mol acetic acid and stirring for 20 min. For the vanadium-containing solution, 1.77 g NH_4VO_3 was dissolved in 100 mL deionized water containing 0.015 mol H_2O_2 by ultrasonic treatment. In a typical spin-coating process, 0.5 mL bismuth-containing solution was first spin-coated on the cleaned FTO glass substrate at 2000 rpm for 15 s, and then spin-coated vanadium-containing on it under the same condition. This process was repeated 15 times. The obtained film was then washed with DI water, followed by a drying step at 50 °C for 10 h, and subsequently annealing at 450 °C for 3 h, the $BiVO_4$ film was finally prepared.

2.3. Preparation of ZrON-C/CF cathode

Preparation of UiO-66-NH_2/CF precursor: UiO-66-NH_2/CF precursor was synthesized through previous work with modification [33]. Typically, the acidifying carbon felt (CF) was vertically placed in a DMF (50 mL) solution containing 0.42 g $ZrCl_4$, 0.42 g 2-aminoterephthalic acid (BDC-NH_2) and 3.3 mL hydrochloric acid, and then heated at 120 °C in Teflon-liner stainless steel autoclave for 48 h. After cooling to room temperature, the obtained UiO-66-NH_2/CF precursor was washed by deionized water and then dried at 80 °C under vacuum. The content of UiO-66-NH_2 on CF was adjust by controlling the concentration of $ZrCl_4$ and 2-aminoterephthalic acid in 50 mL DMF.

Preparation of ZrON-C/CF cathode: The obtained UiO-66-NH_2/CF precursor was placed in a tube furnace and calcined at 550 °C for 2 h with a heating rate of 5 °C/min under Ar atmosphere. A series of ZrON-C_x/CF samples obtained at different content of UiO-66-NH_2 were named as ZrON-$C_{0.5}$/CF, ZrON-C_1/CF and ZrON-C_2/CF. For comparison, the ZrO-C_x/CF cathodes without N were obtained by the carbonization of UiO-66/CF, which were synthesized by $ZrCl_4$ and BDC.

2.4. Characterization

The X-ray diffraction (XRD) patterns were obtained by X′Pert PRO MPD (Panalytical, Netherlands). The morphology of the prepared samples was observed by a field emission scanning electron microscope (FESEM, Hitachi Regulus8100, Japan). Fourier transform infrared (FT-IR) were tested using a Nicolet 6700 IR spectrometer (Thermo Fisher Scientific Co., USA). The surface chemical bonds and components were ascertained by X-ray photoelectron spectroscopy (XPS) (Thermo ESCALAB 250XI, USA). The thermal stability of UiO-66-NH_2 was measured by thermal gravimetric analysis (TGA, Rigaku, Japan) under N_2 flow (20 cm^3/min).

Electrochemical tests were executed in a three-electrode system, in which 0.1 M Na_2SO_4 solution was employed as electrolyte, a Pt sheet was used as counter electrode and an Ag/AgCl electrode was used as reference electrode. The working electrodes were the prepared $BiVO_4$ and ZrON-C/CF. All the electrochemical tests were controlled by an electrochemical workstation (CHI 660e, Shanghai Chenhua Instrument Co., Ltd).

2.5. Construction and evaluation of DEPFC

The DEPFC was assembled by adhering Si photovoltaic cell (PC, function area 4 × 2 cm^2) at the back of $BiVO_4$ film as photoanode, and ZrON-C/CF as cathode. The positive pole of Si PC was connected with $BiVO_4$ by Cu wire and sealed with silicone rubber, and the negative pole was connected with ZrON-C/CF cathode by Cu wire. 20 mg/L uranyl nitrate and 20 mg/L tetracycline hydrochloride (TC) containing 0.1 M

Na_2SO_4 solution was used as the simulated complex wastewater. The pH of the uranium solutions was adjusted using 0.3 M NaOH and HNO_3. A 300 W Xenon lamp (PerfectLight, China) with AM1.5 filter was employed as simulated sunlight (100 mW/cm^2). The solution was stirred vigorously for 40 min in dark to ensure the ad-desorption equilibrium. After stirring for 40 min in the dark and subsequently turning on the light, 1 mL suspension was taken out every 10 min and filtered with a needle filter (pore diameter was 0.22 μm). The degradation rate of TC was analyzed with a High-Performance Liquid Chromatography (HPLC, Agilent 1260, American). The residual of U(VI) concentration was analyzed by an inductively coupled plasma optical emission spectrometer (ICP-OES, 720, Varian, USA).

2.6. DFT calculations

The geometries of the pure carbon material, N/O/Zr doped carbon material and UO_2^{2+} adsorbed on these materials were all optimized with dispersion corrected density functional theory (DFT-D3) at the PBE0-D3/def2-SVP + SDD level using Gaussian program. Here, the SDD effective core potential was used to describe the atomic orbital and relativistic effect of heavy element uranium. The adsorption energy of the complex was calculated from the formular: E(adsorb) = E(A+B) – E (A) – E(B),where E(A) and E(B) is the energy of isolated molecules, E (A+B) is the total energy of the complex structure. The hirshfeld atomic charges from which we can analyze the charge transfer directly were obtained by population analysis from the wave function file of DFT calculation using Multiwfn. The visualization of the frontier molecular orbitals were rendered using Visual Molecular Dynamic program (VMD).

3. Results and discussion

3.1. Characterization of ZrON-C/CF cathode

In this work, the UiO-66-NH_2 derived ZrON-C supported on CF was prepared via a simple two-step process, as schematically displayed in Fig. 1**a**. Initially, the octahedral UiO-66-NH_2 nanoparticles were in situ grown on the carbon fibers of CF directly through a facile hydrothermal method in the presence of Zr^{4+} and BDC-NH_2. The XRD patterns of UiO-66-NH_2-x/CF exhibit a broad diffraction peak at ~23° (Fig. S1), belonging to the (002) facet of graphite structure, and an obvious diffraction peak at ~7.2° assigned to UiO-66-NH_2 also detected, confirming the successful growth of the UiO-66-NH_2 on CF [34]. Fourier transform infrared spectroscopy (FT-IR) results detected the peaks at 1615, 1573, 1492, 1419, and 1254 cm^{-1}, which can be indexed to N-H, C-O, C═C, C-O and C-N bond, respectively (Fig. S2), further confirming the successful preparation of the UiO-66-NH_2 on CF [35]. Afterwards, the MOFs derived ZrON-C on CF was obtained via a simple post-annealing treatment in Ar atmosphere. The thermal stability of UiO-66-NH_2 precursor was obtained by thermo gravimetric analysis

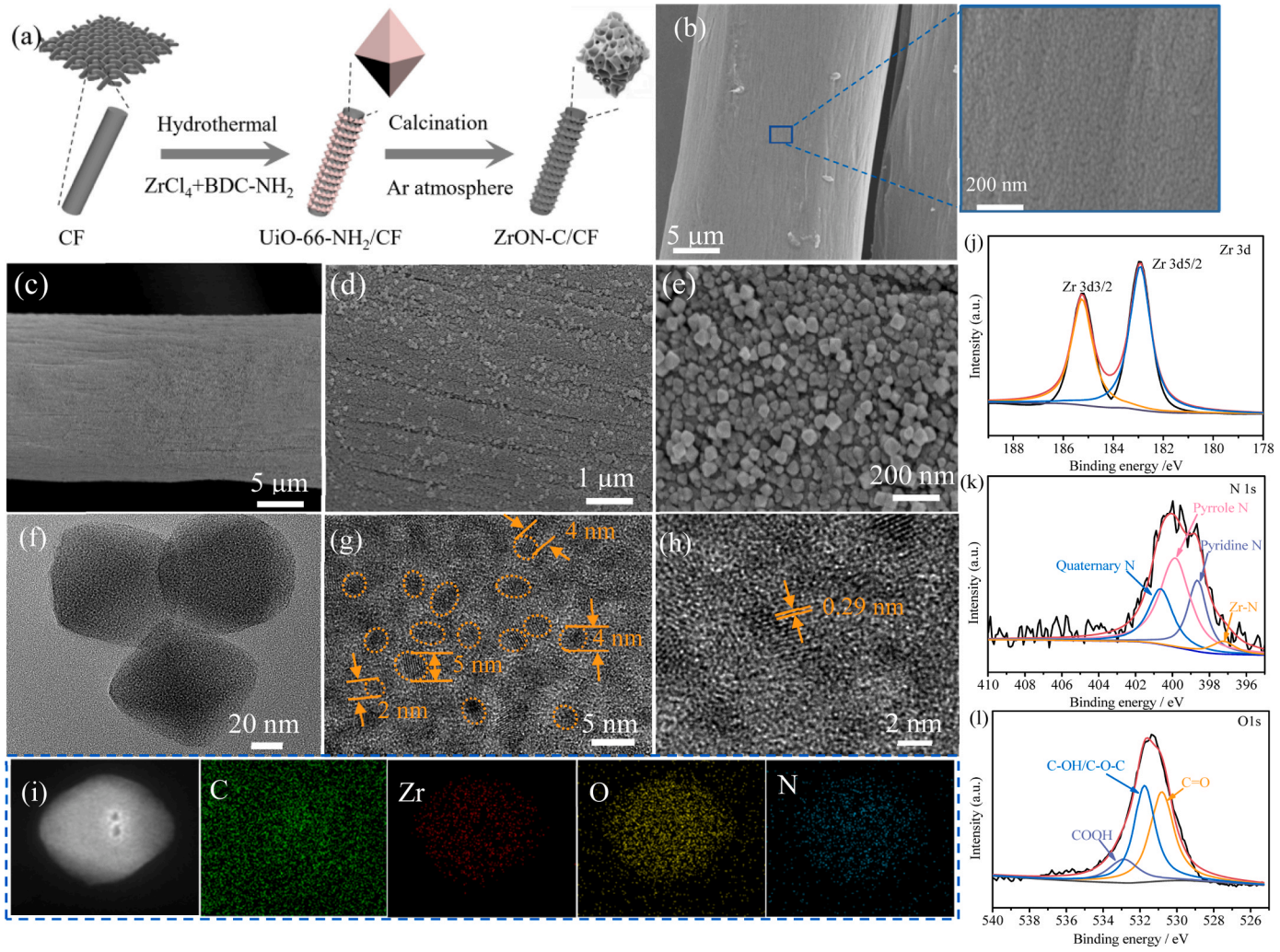

Fig. 1. (a) Schematic illustration for the preparation of UiO-66 derived ZrON-C on CF substrate; SEM images of (b) CF and (c-e) ZrON-C_1/CF under different magnifications; (f-h) TEM images and (i) EDS mapping of ZrON-C; XPS spectra of (j) Zr 3d, (k) N 1 s and (l) O 1 s of ZrON-C_1/CF.

(TGA) in Ar atmosphere (Fig. S3), and three steps of weight loss are observed [36]. The first weight loss is about 7.5 wt% from 50 to 100 °C, which should be ascribed to the initial solvent loss, and the weight loss in the second step is about 18 wt% from 150 to 350 °C, corresponding to the dehydration of the $Zr_6O_4(OH)_4$. The last weight loss is approximate 40 wt% from 375 to 525 °C, which should be attributed to the pyrolysis of the BDC-NH_2. Therefore, 550 °C is chosen as the calcination temperature to ensure the complete carbonization of the MOF precursor. Obviously, the preparation process of the ZrON-C/CF is fairly simple, low-cost and environment friendliness.

The SEM images indicate CF is consisted of interleaved carbon fibres (Fig. S4) and the diameter of fibres is about 20 μm with relatively smooth surface (Fig. 1**b**). The as prepared ZrON-C/CF shows uniformly covered ZrON-C nanoparticles with high density (Figs. 1**c**-1**e**). The magnified SEM image in Fig. 1**e** reveals the ZrON-C nanoparticles well inherit the typical octahedral structure of the UiO-66-NH_2 and the average particle size is about 80 nm. Moreover, uniform and abundant space between individual nanoparticles can also be observed, which can ensure the adequate exposure of the active sites and facile penetration of electrolyte. The sample prepared with a half amount of UiO-66-NH_2 precursor, the sparse ZrON-C is dispersed on the surface of CF fiber (Figs. S5a-5**c**). However, when further increasing the amount of UiO-66-NH_2 precursor to double, the obtained ZrON-C nanoparticles are compactly distributed on the CF fiber surface with few spaces between individual nanoparticles (Figs. S5d-5**f**). EDS analysis elemental mapping revealed the distribution of C, O, N and Zr elements over the entire ZrON-C/CF (Fig. S6). The SEM images of the compared ZrO-C_x derived from UiO-66 are also obtained. As shown in Fig. S7, the morphology of ZrO-C is similar with ZrON-C, indicating the introduction of –NH_2 does not affect the morphology of UiO-66.

The TEM image of ZrON-C derived from the pyrolysis of UiO-66-NH_2 shows that the size and polyhedron shape of the original MOF crystals are well reserved in the corresponding pyrolyzed samples (Fig. 1**f**). HRTEM images (Fig. 1**g**) reveals ZrO_2 nanospheres with a particle size of 5 ± 3 nm are uniformly doped in porous carbon sketch. Furthermore, the ZrO_2 nanospheres exhibits a distinct lattice spacing of 0.29 nm (Fig. 1**h**), matching well to the (111) crystal face of ZrO_2 [37]. The EDS element mappings further observe that C, Zr, O and N are homogeneously distributed in a single ZrON-C particle (Fig. 1**i**). However, no obvious diffraction peak of ZrO_2 is detected in XRD patterns (Fig. S8), which is possibly due to the low content and high distribution of Zr species [38].

XPS analysis further indicates the presence of C, Zr, N and O elements in the sample (Fig. S9). The C 1 s spectrum has been split into four peaks, of which 284.5 and 285.2 eV can be corresponded to the sp^2 and sp^3 C-C bonds from carbon-containing organic ligands (Fig. S10). Meanwhile, the other two peaks located at 285.7 and 288.3 eV can be assigned to the C-N and C═O, suggesting that the N and O in UiO-66-NH_2 are successfully doped into the derived porous carbon. In the high-resolution Zr 3d spectrum (Fig. 1**j**), two characteristic peaks at 182.9 eV and 185.5 eV should be ascribed to Zr 3d5/2 and Zr 3d3/2, respectively [37], which manifests that Zr exists in the oxidation state + 4 in ZrON-C/CF. As to N1s spectrum (Fig. 1**k**), pyridinic nitrogen (398.7 eV), pyrrole nitrogen (399.9 eV), and quaternary nitrogen (400.8 eV) are observed [26]. Pyridinic nitrogen and pyrrole nitrogen can act as the functional groups in the electrochemically active site [39,40] and enhance the U(VI) reduction activation. Quaternary nitrogen is bonded with three sp^2 carbon atoms in the inside of the graphitic carbon plane, which is beneficial to improve the electric conductivity of the graphitic carbon because of the significant change in the electron-donor feature [41]. Importantly, N doping can improve the hydrophilia of the carbon material [42], which favors the interfacial reaction in aqueous system. Another peak located at 397.2 eV should be assigned to Zr-N [31], which could be ascribed to partially doping of Zr in the N doped carbon matrix. The high-resolution O1s spectrum can be deconvoluted into three peaks: the binding energies of 530.8, 531.7, and 533.0 eV are indexed to carbonyl groups (C═O), hydroxylic groups (C-OH) or ether groups (C-O-C), and carboxyl groups (COOH) (Fig. 1**l**). As with the N doping, the introduction of O can improve the hydrophilia to decrease the inert surface area and provide amount of active sites. Specifically, the C-OH hydroxyl groups are beneficial to the moistening of the carbon material and the existence of C-O in the COOH can enhance the surface acidity [41]. The plenty of N and O containing groups and carbon matrix would enable the ZrON-C/CF with high activity in UO_2^{2+} adsorption and reduction.

3.2. Characterization of $BiVO_4$ photoanode

A $BiVO_4$ film prepared by a simple spin-coating method is employed as the photoanode material. As shown in Fig. 2**a**, it can be seen that $BiVO_4$ film is rugged and tightly connected with FTO and the average thickness is about 100 nm. The XRD pattern (Fig. 2**b**) demonstrates that $BiVO_4$ is monoclinic scheelite [43]. XPS survey indicates the presence of Bi, V and O elements (Fig. S11). The high-resolution XPS spectrum of Bi 4 f (Fig. 2**c**) displays the Bi 4 $f_{7/2}$ and Bi 4 $f_{5/2}$ peaks at 158.3 eV and 163.6 eV, respectively, indicating the presence of Bi^{3+}. The V 2p spectra (Fig. 2**d**) shows the peaks at 519.9 eV and 523.4 eV, indicating the + 5 oxidation state of V. The high-resolution O 1 s XPS spectrum indicates two O 1 s peaks at 529.0 and 531.1 eV (Fig. 2**e**), which should be assigned to the lattice oxygen and surface hydroxyl groups. These results indicate the successful synthesis of uniform $BiVO_4$ film of FTO substrate. Under AM 1.5 illumination, the chopped LSV plot displayed in Fig. 2**f** confirms the monolithic $BiVO_4$ photoanode possesses an excellent photochemical activity with the photocurrent density of 2.0 mA cm^{-2} at 0.8 V versus Ag/AgCl. A stable photocurrent density of 1.83 mA cm^{-2} in 400 s with no obvious decay is also obtained (Fig. S12), and the Ohmic impedance and interfacial charge-transfer impedance was as low as 155.7 Ω and 39.5 Ω, respectively, which indicated the superior conductivity of $BiVO_4$ photoanode (Fig. S13).

3.3. Simultaneous organic degradation and uranium recycling by DEPFC

Radioactive wastewater always contains organic matters derived from the nuclear fuel manufacturing process. Additionally, uranium contaminated water bodies also invariably contain organics due to the extensive use of pesticides, antibiotics, drugs, etc., and the illegal discharge of pollutants [44–46]. Due to the unsaturated coordination structure of uranyl ions (UO_2^{2+}, typically stable and soluable uranium species in water), the organic matters can coordinate with UO_2^{2+}, which poses a significant challenge for uranium removal, and also presents a significant threat to the ecosystem. To achieve efficient uranium and organic removal, a drivingpowers enhanced photocatalytic fuel cell (DEPFC) was proposed to by using the as-prepared $BiVO_4$ photoanode and ZrON-C/CF cathode for simultaneous uranium reduction and organic oxidation. The detailed construction of DEPFC can be found in the Experimental section. As a widely utilized antibiotic, TC is used as the model organic matter.

First, the removal performance of the single U(VI) solution over DEPFC is assessed as shown in Fig. 3**a**. The photolysis of U(VI) is only ~2.5% after 40 min of illumination. Under dark conditions (no extra energy field), the adsorption removal ratio of ZrON-C_1/CF is about 1.5 times higher than that of pure CF due to the more active sites exposure. After the DEPFC is fabricated, the performances of U(VI) removal are obviously enhanced, and the DEPFC system with ZrON-C_1/CF cathode displays the highest removal efficiency of 99.2% after 40 min operation with a reaction rate constant (k) of 0.115 min^{-1}, which is about 4.3 time that of CF cathode (Fig. 3**b**). In addition, compared with ZrO-C_x/CF cathode, the ZrON-C_x/CF cathodes show a better U(VI) removal ratio, indicating the positive effect of N species on U(VI) removal. As to the model wastewater with only TC, similar activity tendencies are also observed, and the ZrON-C_1/CF cathode shows the optimal degradation efficiency with a removal ratio of 99.1% (Fig. 3**c**) and a k value of

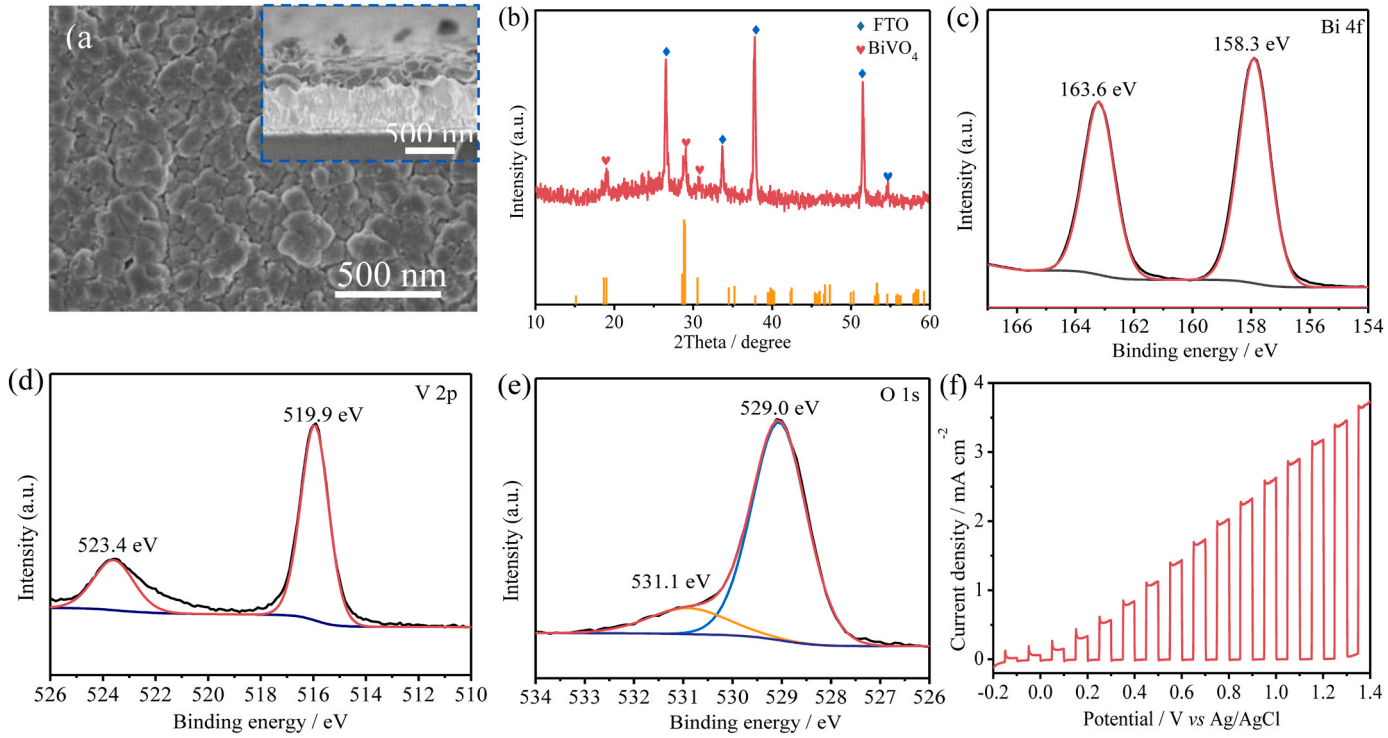

Fig. 2. (a) SEM image, (b) XRD pattern, (c-e) Bi 4 f, V 2p and O 1 s XPS spectra, and (f) chopped LSV curve (tested in 0.1 M Na_2SO_4 under AM1.5 illumination) of $BiVO_4$ photoanode.

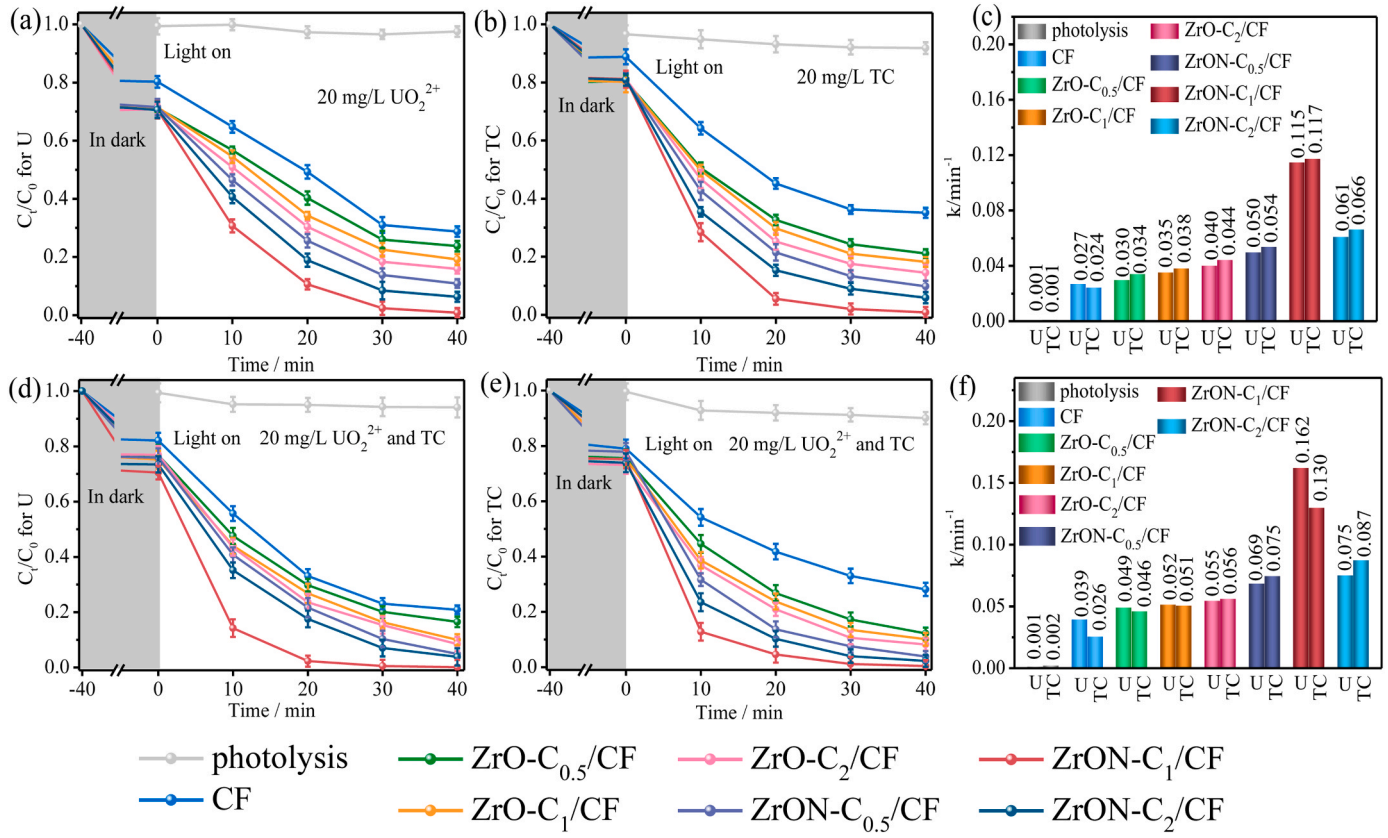

Fig. 3. The removal ratio of (a) UO_2^{2+} and (b) TC in their individual solutions; (c) The corresponding *k* values; The removal ratio of (d) UO_2^{2+} and (e) TC in their coexisting solutions; (f) The corresponding *k* values.

0.117 min^{-1} (Fig. 3**d**), further confirming the excellent photoelectrocatalytic activity of the ZrON-C_1/CF cathode in DEPFC system.

When treating model wastewater with both U(VI) and TC, the existence of TC can positively affect the elimination of U(VI) (Fig. 3**e**), and the DEPFC system with ZrON-C_1/CF cathode can eliminate 99.9% of U (VI) in 40 min with a k value increased from 0.115 to 0.162 min^{-1} (Fig. 3**f**). The enhanced removal performance probably due to the holes in $BiVO_4$ photoanode can be easily consumed by TC, which restrains the recombination of the electrons and holes, resulting in enhanced reduction of U(VI) by photoexcited electrons [47]. In the same way, the U(VI) reduction consumes the photoexcited electrons, which in turn benefits the TC degradation with the k value increased from 0.117 to 0.130 min^{-1} (Figs. 3**g** and 3**h**). Compared to the system with CF, the k values are improved ~4.2 and ~5.0 times for U(VI) and TC, respectively, when using ZrON-C_1/CF cathode, demonstrating the superior activity of ZrON-C_1/CF cathode in DEPFC for both U(VI) reduction and organic oxidation. Additionally, excellent performance of the DEPFC is also achieved in treating model complex wastewater with a wide range of initial concentration (5–40 mg/L), and the removal ratios are higher than 90% within 40 min (Fig. S14). The synergistic effect of U(VI) and TC removal illustrates the excellent adaptability of the DEPFC system to such organics-containing complex U(VI) wastewater.

3.4. Effects of pH and electrolyte concentration on organic degradation and uranium recycling by DEPFC

It is well known that the solution pH affects the dissociation state of pollutants, the surface charge of electrodes and the formation of active free radicals, thereby determining the photoelectrocatalytic efficiency [48]. As is displayed in Figs. 4**a** and 4**b**, both the removal efficiencies of UO_2^{2+} and TC by DEPFC reach the maximum at pH = 7.0. Under acidic condition, TC is mainly protonated to cation state TC^+, thus restraining the interaction between TC^+ and positive charged photoanode [49]. The removal rate of U(VI) (Fig. 4**c**) in acid environment is decreased due to the abundant H^+ competed with UO_2^{2+} for electrons at the cathode, leading to the decline in the performance of the DEPFC system [50]. However, the removal of UO_2^{2+} began to decrease when pH> 7 (Fig. S17a), which is probably because the deposited hydrolytic precipitation of UO_2^{2+}, leading the weak adsorption of U on the cathode surface. In addition, under the alkaline conditions, UO_2^{2+} primarily existing in the form of negatively charged $[(UO_2)_3(OH)_7]^-$ and $[(UO_2(OH)_3]^-$ (Fig. S15). The negatively charged U(VI) generates electrostatic repulsion with cathode, which weakens its adsorption on the material and decrease its reduction efficiency. As for the degradation of TC, the removal rate increases slightly when pH> 7 (Fig. S17b), which can be attributed to the electrostatic attraction between positively charged anode and TC since TC mainly existed in the form of TCH^- and

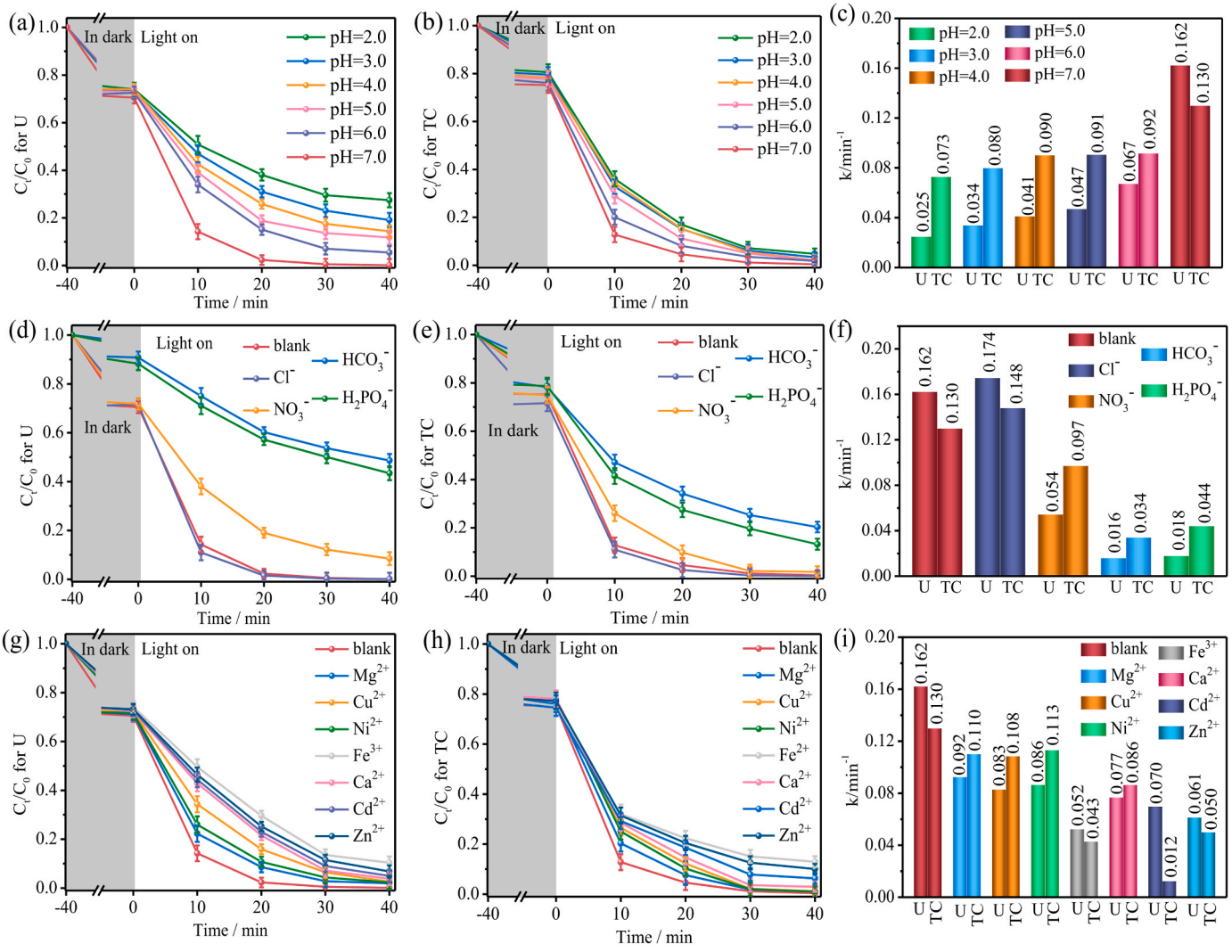

Fig. 4. The effects of pH (a, b), anions (d, e) and cations (g, h) and corresponding *k* values (c, f and i) on the removal of UO_2^{2+} and TC by DEPFC under AM 1.5 illumination.

TC^{2-} under alkaline conditions [51]. In spite of this, it is worth noting that DEPFC system still possesses a removal efficiency of > 85% both for UO_2^{2+} and TC in the pH range of 2–7, indicating the proposed DEPFC is suitable for varying acidity wastewater.

In the DEPFC, the inner resistance derived from the model wastewater affects the charge transfer in the DEPFC system. Undoubtedly, the removal rates of UO_2^{2+} and TC are enhanced when increasing the electrolyte (Na_2SO_4) concentration from 0–0.5 M (Fig. S16). However, the removal ratios still reach 88% and 73% for UO_2^{2+} and TC, respectively, when without of Na_2SO_4, suggesting the superior activity of DEPFC in organic oxidation and UO_2^{2+} reduction. After increasing the Na_2SO_4 concentration from 0.1 and 0.5 M, the k values are slightly increased for both U(VI) and TC, which should be due to the change of governing factor from inner resistance to others, like mass transfer. Nonetheless, the DEPFC has a great potential in treating wastewater with salts under a wide range.

3.5. Effects of co-existed ions on organic degradation and uranium recycling by DEPFC

Inorganic ions are unavoidable existed in actual wastewater and natural water, which may influence the removal efficiency of target contaminants. Therefore, we further explore the influence of various inorganic anions and metal cations on UO_2^{2+} and TC removal in DEPFC. As shown in Figs. 4**d** and 4**e**, Cl^- shows a slightly positive effect on both UO_2^{2+} reduction and TC decomposition with k values of 0.174 and 0.148 min^{-1} (Fig. 4**f**), respectively. This should be due to the oxidation of Cl^- by h^+ (e.g., formation of Cl• and HOCl) that facilitates the charge separation in $BiVO_4$ photoanode. However, the removal rates of UO_2^{2+} and TC are reduced in the presence of oxygen-containing anions, e.g., NO_3^-, HCO_3^- and $H_2PO_4^-$, which is mainly caused by the coordination effect that causes the formation of complexes, e.g., $UO_2(NO_3)_2OH^-$, $UO_2(HPO_4)_2^{2-}$, $(UO_2)_2CO_3(OH)_3^-$ and UO_2HPO_4 [52–54]. The negative charged complexes reduce the adsorption of U(VI) then further diminish its reduction efficiency. As for the oxidative degradation of TC, h^+ and •OH on photoanode could react with HCO_3^- to produce carbonate radical ($CO_3•^-$) in the presence of HCO_3^- [55]. However, the oxidizing ability of $CO_3•^-$ is extremely weak, resulting in a significant decay in degradation of TC. In addition, $H_2PO_4^-$ also has a strong inhibition effect, which may be due to the fact that $H_2PO_4^-$ can adhere to the surface of the photoanode as a chelating agent and form a solid-liquid phase barrier [56].

Different from the inorganic anions, transition metal cations possesses different levels of negative influence on the reduction of UO_2^{2+} owing to the competition effect (Fig. 4**g**). The effect of Fe^{3+} is relatively obvious than other divalent metal cations, which could be credited to the excess electrons in trivalent Fe^{3+} [57]. Additionally, the bigger hydrated radius, the more preferentially bound, thus, the effect degree of various metal cations is closely relevant to their hydrated radius: Fe^{3+} (0.480 nm) > Zn^{2+} (0.430 nm) > Cd^{2+} (0.426 nm) > Ca^{2+} (0.420 nm) > Cu^{2+} (0.419 nm) > Ni^{2+} (0.404 nm) > Mg^{2+} (0.300 nm) [57]. Besides, the double electron layer of adsorbent (ZrON-C cathode) would be compressed by cations with large hydrated radius, resulting in the decrease of active sites and consequently decreasing the reduction performance [58]. As for the degradation of TC, the removal efficiency and rates (Fig. 4**h and i**) are also slightly reduced in the presence of metal cations, which could be ascribed to the possible coordination between metal cations and TC that limits the interaction between TC and h^+ [55]. Even so, excellent removal rates for both UO_2^{2+} (> 90%) and TC (> 88%) are achieved for DEPFC under a wide range of inorganic ions.

3.6. Application perspective of DEPFC

In addition ot TC, the efficiency of the DEPFC in simultaneously removing different organic compounds and UO_2^{2+} is further evaluated. As shown in Figs. 5**a and** 5**c**, the removal efficiency of UO_2^{2+} is affected slightly by different organic compounds with the values higher 95%, demonstrating the excellent extraction performance of ZrON-C/CF

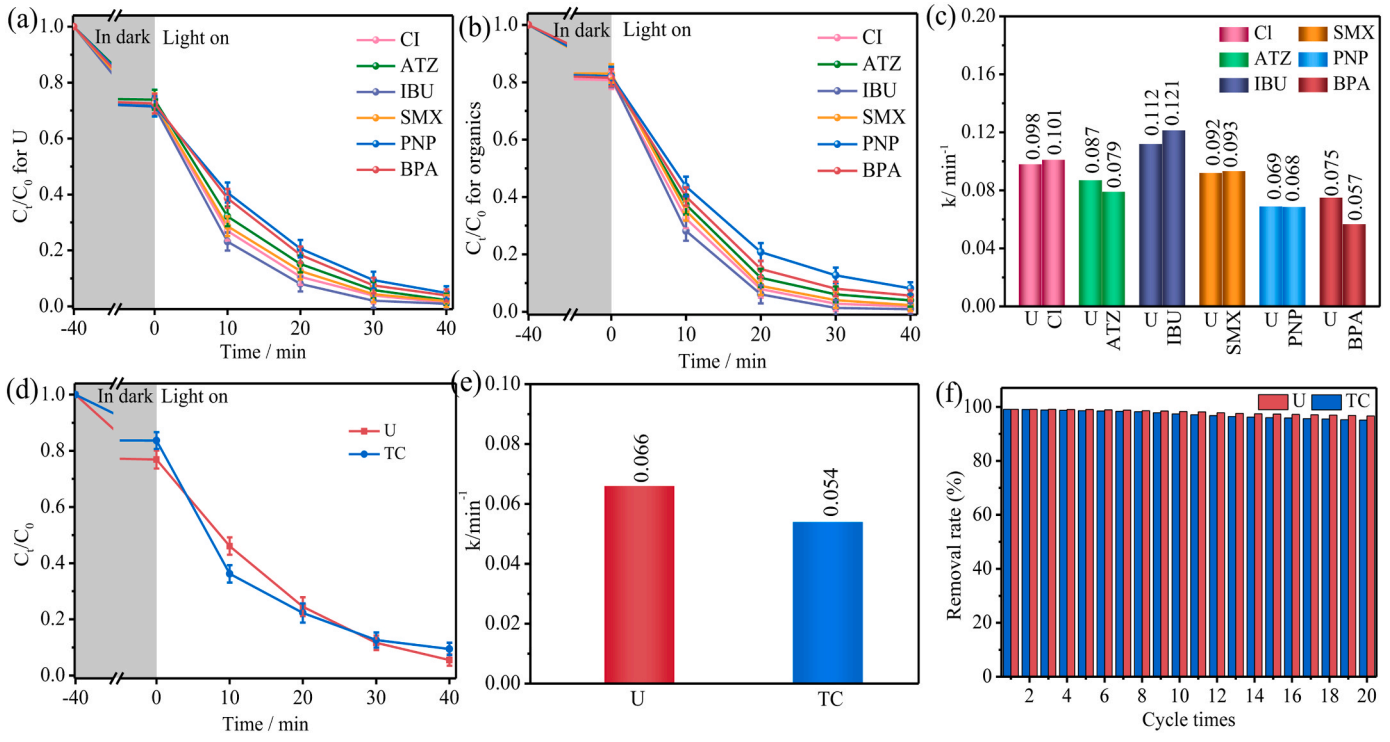

Fig. 5. The performance of DEPFC in simultaneously removing (a) UO_2^{2+} (20 mg/L), (b) different organics (20 mg/L) and (c) corresponding *k* values; (d) removal rates of UO_2^{2+} and TC by DEPFC from simulated sea water (Cl^-: 0.988 mol/L, Na^+: 0.459 mol/L, Mg^{2+}: 0.279 mol/L, K^+: 0.01 mol/L, Ca^{2+}: 0.01 mol/L, SO_4^{2-}: 0.027 mol/L, HCO_3^-: 0.002 mol/L, Br^-: 0.003 mol/L) and (e) corresponding *k* values; (f) the recycling tests of the proposed DEPFC system.

cathode in DEPFC for UO_2^{2+}. Additionally, all the model organic pollutants, e.g., ibuprofen (IBU), ciprofloxacin (CI), sulfamethoxide (SMX), atrazine (ATZ), bisphenol A (BPA) and p-nitrophenol (PNP), are effectively degraded with removal ratios higher than 92% under AM 1.5 illumination (Fig. 5**b**), further revealing the outstanding oxidation property of DEPFC.

In order to evaluate the applicability of this DEPFC system for extracting uranium in complicated ocean environment, we further explored the extraction capacity of UO_2^{2+} in stimulated seawater. As shown in Figs. 5**d**, 91.7% of initial ~5 ppm UO_2^{2+} in the simulated seawater can be extracted and 88.2% of initial ~5 ppm TC can be simultaneously degraded after 40 min operation with a removal rate constant of 0.066 and 0.054 min^{-1} (Fig. 5**e**), respectively, which suggests the potential of applying this technology for highly efficient uranium extraction and organic pollutants degradation from complicated seawater. Fig. 5**f** and Table S1 shows the cycling performance of DEPFC on UO_2^{2+} and TC removal. After 20 cycle runs, there are no obvious decay for the removal rates of UO_2^{2+} and TC, which confirms that the proposed DEPFC system exhibits high activity and excellent stability for the UO_2^{2+} reduction and simultaneous organics degradation.

3.7. Possible mechanism of DEPFC

The Electrochemical impedance spectroscopy (EIS) plots (Fig. 6**a**) shows the ZrON-C_1/CF had the smallest semicircle diameter, indicating the ZrON-C_1/CF possesses superior conductivity to other cathodes. Obviously, the semicircle of ZrO-C_1/CF is slightly lower than that of pure CF, and the semicircle of ZrON-C_1/CF is significantly decreased than that of ZrO-C_1/CF, manifesting that the introduction of Zr, N and O can reduce the charge transfer resistance, which is conducive to carriers transfer and separation, and finally improve the charge transfer property in DEPFC. Cyclic voltammetry curves (CV) curves (Fig. 6**b**) displays the ZrON-C_x/CF cathodes exhibits markedly enhanced current density as compared with the pure CF cathode, which can be attributed to the more efficient charge transfer and increased active sites. Obviously, ZrON-C_1/CF cathode reveals the highest current density, which in agreement with the analysis of EIS. Fig. 6**c** shows the linear scanning voltammetry (LSV) curves of different cathodes. The bare CF cathode exhibits very limited catalytic reduction activities, while ZrON-C_x/CF cathodes shows significantly improved catalytic performance. At the current density of 10 mA cm^{-2}, the overpotentials for CF, ZrO-C_1/CF, ZrON-$C_{0.5}$/CF, ZrON-C_1/CF and ZrON-C_2/CF are observed to be − 285, − 274, − 266, − 198 and − 221 mV respectively. Obviously, all ZrON-C_x/CF cathodes demonstrate much higher catalytic reduction performance than both CF and ZrO-C_1/CF.

To study the mechanism of TC degradation on photoanode, free-radical capture experiments and electron paramagnetic resonance (EPR) tests were then performed. After adding TBA (scavenger of •OH) and EtOH (scavenger of h^+), the removal efficiencies of TC are 61.32% and 41.08%, respectively (Fig. 6**d**), which manifests that both h^+ and •OH contribute to the decomposition of TC. As shown in Fig. 6**e**, TEMPO-h^+ signal with the peak intensity of 1:1:1 is detected under visible-light irradiation, demonstrating the generation of h^+. Meanwhile, the signals of DMPO-•OH with the intensity of 1:2:2:1 appears under visible-light irradiation (Fig. 6**f**), proving the generation of •OH in the DEPFC [59]. This result further demonstrates the oxidation of TC is derived from h^+ and •OH in DEPFC under light illumination.

In general, for the heterogenous reaction such as catalytic reduction of U(VI), the initial step is adsorption of UO_2^{2+} onto the specific sites of material, then interfacial reaction converts U(VI) to U(IV) [60]. Therefore, to understand the enhanced mechanism of the ZrON-C_x/CF cathodes for reducing the UO_2^{2+}, water contact angle measurements and density functional theory (DFT) calculations were executed. Fig. S18 and **Video S1** show the contact angle of water on surface of the pure CF, ZrON-C_1/CF and ZrO-C_1/CF cathode. Both the wetting angles of ZrON-C_1/CF and ZrO-C_1/CF (<5°) are smaller than the pure CF (125°), indicating that the ZrO_2 introduction can enhance the hydrophilia of the ZrON-C_1/CF and benefit for the adsorption of UO_2^{2+} onto the specific sites of ZrON-C_1/CF cathode [61].

The behavior of electrons in ZrON-C/CF cathode was first revealed by DFT calculations. As shown in Figs. 7**a** and 7**b**, the Fermi level (EF) of ZrO_2 and N-doped C were calculated to be − 2.462 eV and − 4.776 eV, respectively. The electrons on ZrO_2 would spontaneously transfer to N-doped C to equilibrate the EF difference [62]. The interfacial reaction between UO_2^{2+} and ZrON-C/CF cathode were also disclosed by DFT calculations. As shown in Fig. 7**c**, UO_2^{2+} mainly adsorbed on the CF cathode by Vander Waals force and the distance between U and C structure is about 4.01 Å. As for ZrON-C/CF cathode, UO_2^{2+} mainly coordinated with N atoms in ZrON-C and the distance between U and N is 2.47 Å, which is smaller than that for pure CF cathode, indicating higher

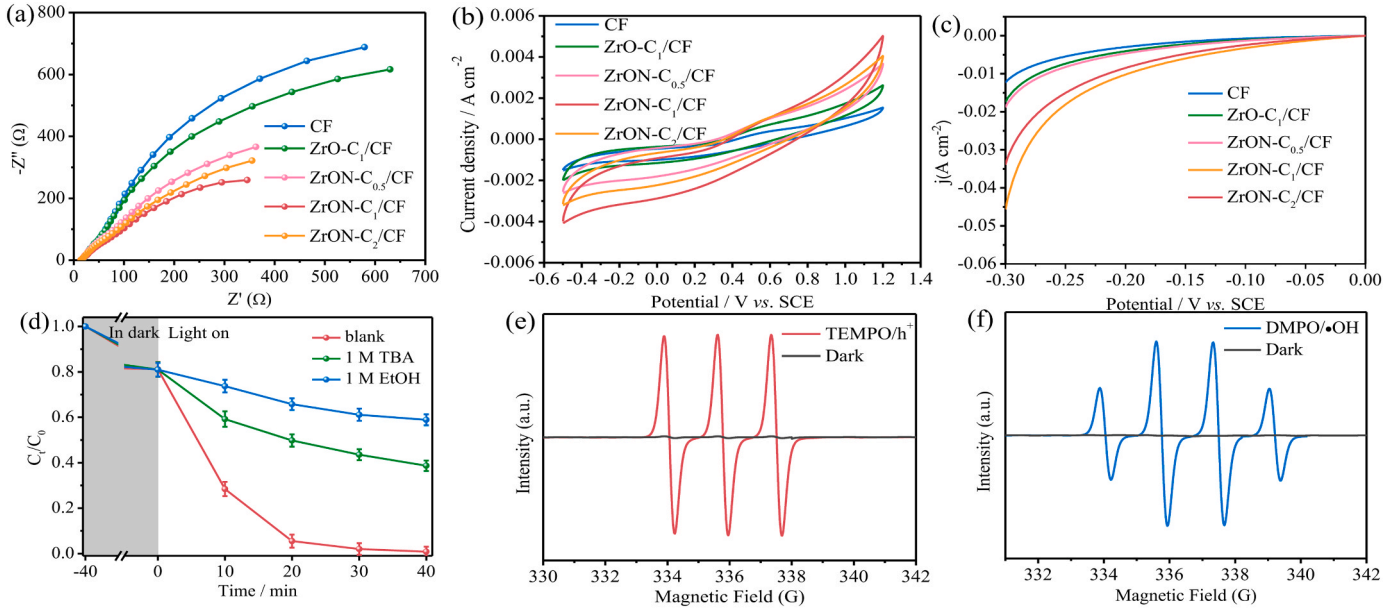

Fig. 6. (a) EIS; (b) CV and (c) LSV curves of different cathodes; (d) scavenger experiment of on the degradation of TC; (e) ESR detection of h^+ and (f) •OH of DEPFC under dark or visible-light (> 420 nm) illumination.

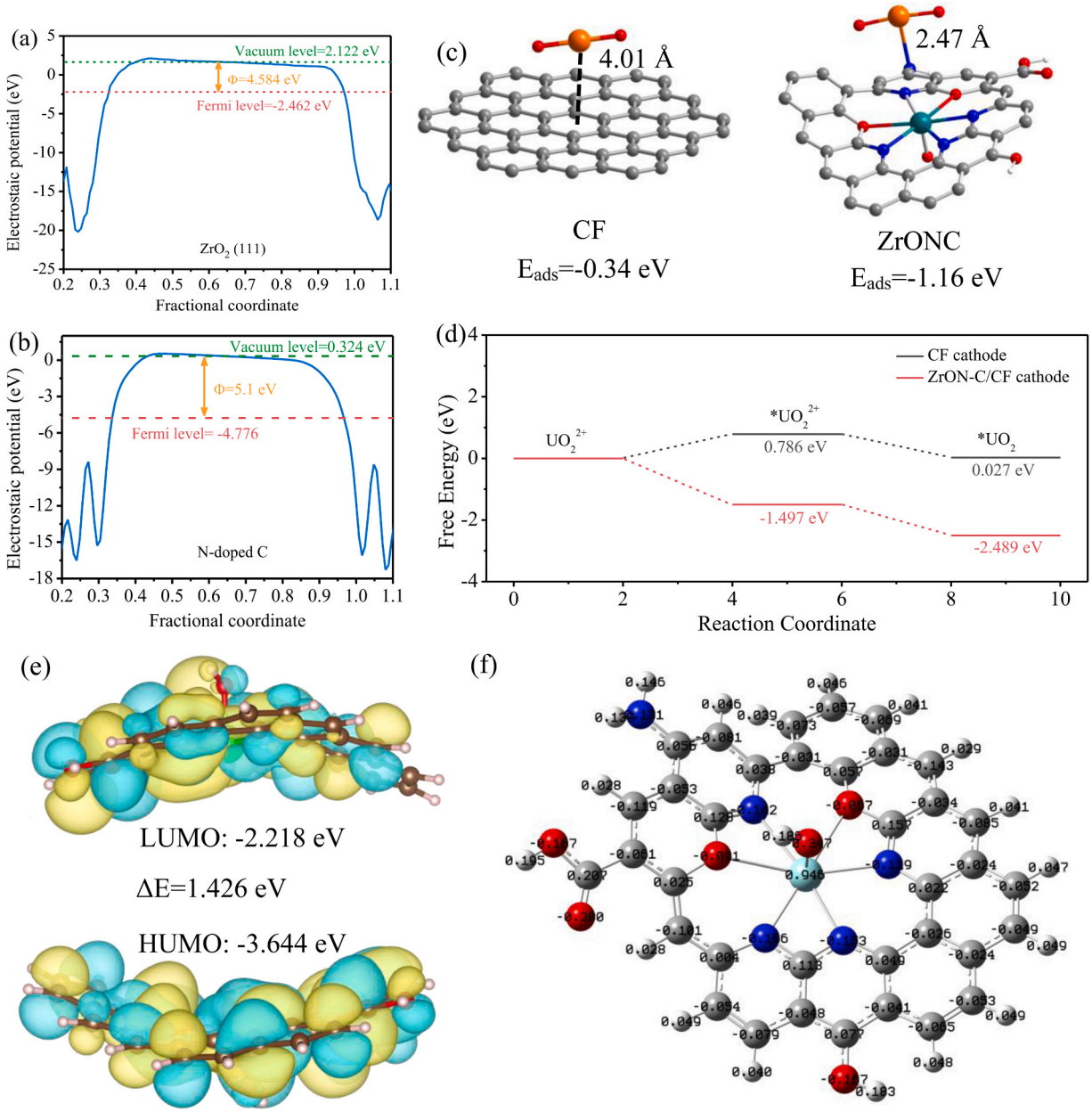

Fig. 7. The work function of (a) ZrO_2 (111) and (b) N-doped C; (c) DFT calculations on adsorption of UO_2^{2+} on various cathodes: the adsorption energy of UO_2^{2+} on (c) pure CF and ZrON-C/CF cathode; (d) The relative free energy of UO_2 formation on pure CF and ZrON-C/CF cathode; (e) HOMO-LUMO energies of the ZrON-C after adsorption of uranium and (f) Hirshfeld charge distribution in ZrON-C.

affinity of ZrON-C/CF cathode to UO_2^{2+}. Besides, ZrON-C/CF also shows a more negative adsorption energy ($E_{ads} = -1.16$ eV) than pure CF ($E_{ads} = -0.34$ eV), also demonstrating the stronger adsorption capacity of UO_2^{2+} by ZrON-C/CF cathode. Fig. 7**d** compares the reaction free energy of UO_2 formation on ZrON-C/CF and pure CF. The coordination of UO_2^{2+} on ZrON-C/CF significantly lowers the reaction energy of $*UO_2^{2+}$ intermediate (−1.497 eV) compared with that on CF (0.786 eV). Subsequently, the $*UO_2^{2+}$ on ZrON-C/CF is reduced by two electrons to form UO_2 with the reaction free energy decreased to − 2.489 eV, indicating that UO_2^{2+} can be spontaneously reduced on the ZrON-C/CF surface [63].

Fig. 7**e** is the HOMO and LUMO energy of the ZrON-C after adsorption of UO_2^{2+}. The result shows that the calculated band gaps of the ZrON-C after UO_2^{2+} adsorption is 1.426 eV. From the top view of the LUMO (Fig. S19), it can be seen that the C-N in ZrON-C contributes more to LUMO, proving that C-N can be used as the reduction active center [64]. In addition, the Hirshfeld charge (Fig. 7**f**) displays that the N atom in ZrON-C is more inclined to gather electrons, which indicated that the introduction of N benefit for charge migration from Zr to C and further to N. The negative atoms can be regarded as the reduction reaction sites, which contribute to the adsorption of UO_2^{2+}. The electron acceptor role of N made it function as the reaction active sites, on which UO_2^{2+} reacted with the electrons to form UO_2. The basic sites of formed -NH_2 groups on ZrON-C can benefit the accumulation of UO_2^{2+} on ZrON-C/CF cathode.

After fixed uranium in DEPFC, there are plenty of coverings on the surface of ZrON-C_1/CF cathode compared with the before reaction (Figs. 1**d** and 8**a**). The corresponding EDS mapping (Fig. 8**c**) indicates that the coverings are uranium compounds. After washed by $NaHCO_3$ (Fig. 8**b**), most part of the coverings is washed off, and there are no obvious changes in the morphology of ZrON-C_1/CF cathode, indicating a good mechanical stability.

XPS analysis shows the presence of U4f peak in survey spectrum

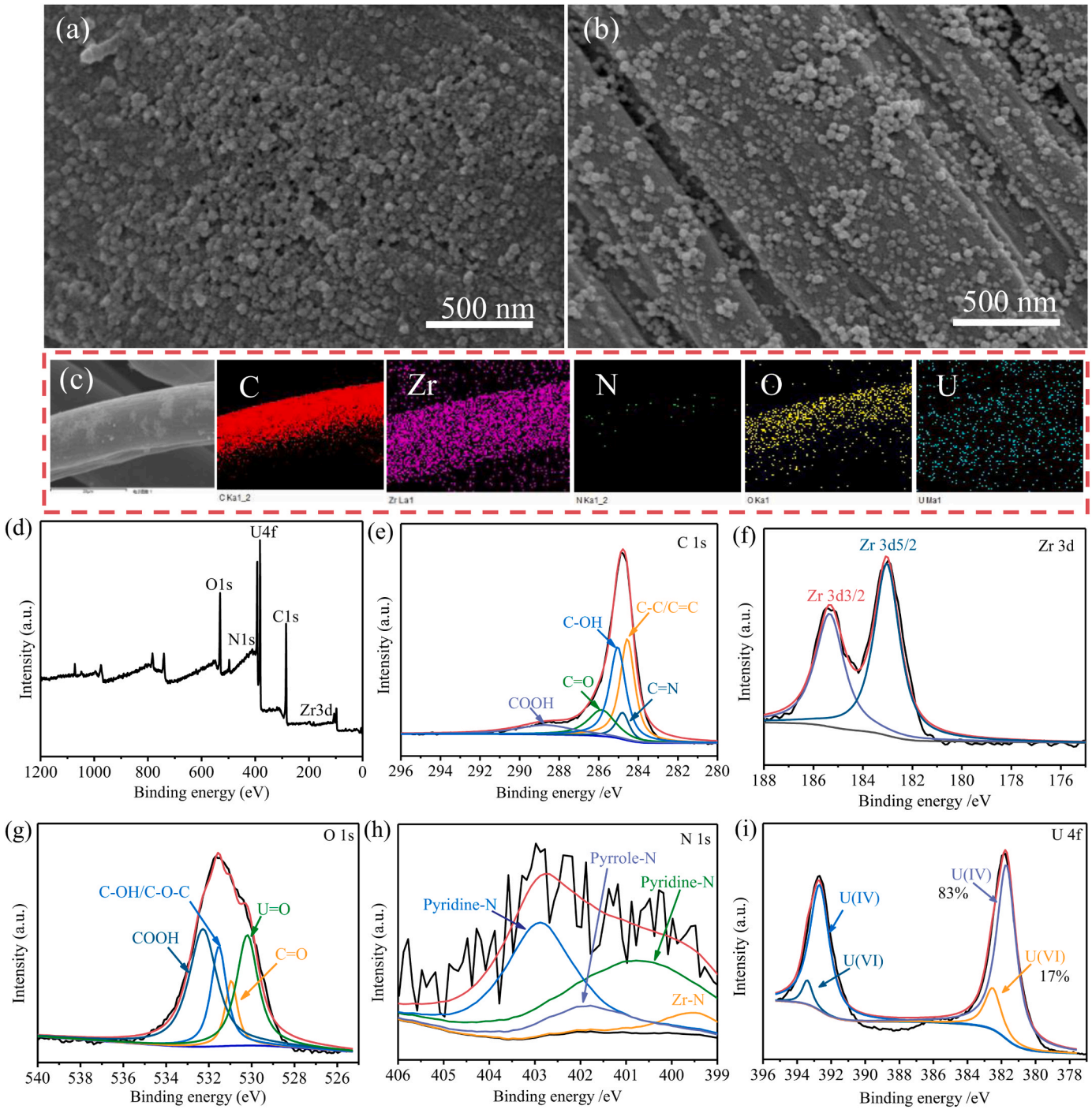

Fig. 8. SEM of ZrON-C_1/CF cathode (a) after fixed uranium in DEPFC and (b) after washed by 0.1 M $NaHCO_3$; (c) EDS elemental mapping, (d) XPS survey of used ZrON-C_1/CF, (e) C 1 s, (f) Zr 3d, (g) O 1 s, (h) N 1 s and (i) U 4 f of ZrON-C_1/CF cathode after fixed uranium in DEPFC.

(Fig. 8**d**), further confirming the existence of U on cathode after operating in DEPFC. Fig. 8**e~8 h** are the high-resolution XPS spectra for C 1 s, Zr 3d, O 1 s and N 1 s, which are similar with the pristine ZrON-C_1/CF, illustrating its excellent chemical stability. It should be noted that a new peak at 530.5 eV appeared in O 1 s spectrum, which can be ascribed to uranium oxide (U═O) [8]. The high-resolution XPS spectrum of U 4 f (Fig. 8**i**) shows that uranium species include both U(VI) and U(IV), and the ratio of U(IV) is as high as 83%, suggesting that a majority of adsorbed U(VI) on ZrON-C_1/CF cathode is reduced to U(IV) in DEPFC. Therefore, this result indicates the proposed DEPFC performs an outstanding stability and excellent activity for UO_2^{2+} reduction.

Based on the above analysis, the possible mechanism of the DEPFC for simultaneously UO_2^{2+} reduction and organic degradation is proposed in Fig. 9. When incoming sunlight from the photoanode side, the $BiVO_4$ photoanode absorbs short wavelength light to generate electrons and holes, and the back silicon photovoltaic cell (PC) absorbs the transmission light to produce bias potential to promote the migration of electrons in $BiVO_4$ photoanode to the ZrON-C_1/CF cathode. The holes are retained in photoanode to oxidized the organic pollutants directly or indirectly by forming highly oxidative •OH ($h^+ + H_2O \rightarrow$ •OH + H^+), while the electrons are transferred to cathode to reduce the UO_2^{2+} into low valence uranium species [65]. In ZrON-C_1/CF cathode, due to the

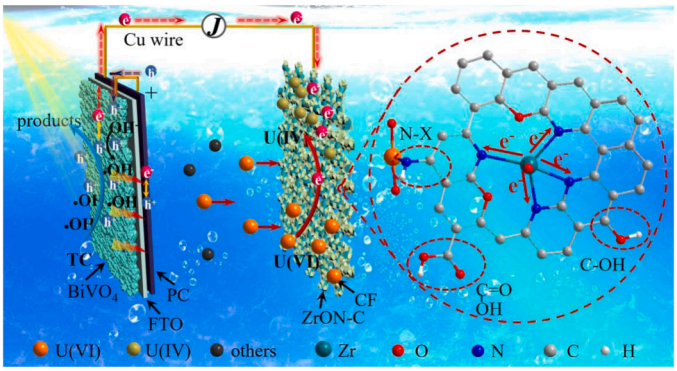

Fig. 9. Possible mechanism for simultaneous pollutant degradation and UO_2^{2+} reduction in the DEPFC.

high work function, N-doped C encourages the transfer of electrons from ZrO_2 semiconductor to N sites [66], thereby promoting efficient transfer of electrons and enhancing reduction efficiency of UO_2^{2+}. Besides, ZrO_2 can improve the wettability thus increases the contact between UO_2^{2+} and cathode. Moreover, N-doping can also increase the variety and number of nitrogen-containing functional groups, thus improving the preferential adsorption ability of ZrON-C_1/CF cathode to UO_2^{2+}. In addition, the presence of O in C structure can also improve the wettability of ZrON-C_1/CF cathode, for instance, the C-OH is beneficial to the wetting of the cathode and the existence of C═O can enhance the surface acidity, and thereby facilitating its reduction performance. To further verify the mechanism, FTIR spectra and XRD analysis have been conducted. Fig. S20a presented the FTIR of ZrON-C_1/CF cathode before and after the reaction. After the reaction, two peaks at 605 and 920 cm^{-1} originated from O═U═O antisymmetric vibration is observed in ZrON-C_1/CF cathode, demonstrating the generation of new uranium-bearing species on the ZrON-C_1/CF surface [67]. XRD analysis displayed in Fig. S20b revealed the presence of uranium-bearing species is UO_2 (PDF#65–0285). Consequently, under sunlight illumination, organic pollutants and uranium can be eliminated simultaneously by the DEPFC.

4. Conclusion

In summary, a novel DEPFC system was designed by using a UiO-66-NH_2 derived ZrON-C/CF cathode and a composite photoanode consisted of a $BiVO_4$ film and a rear-mounted SC. The performance of the DEPFC system is evaluated by simultaneously removing UO_2^{2+} and various organic pollutants. At the optimized condition, the DEPFC can remove almost 100% of UO_2^{2+} and simultaneous degrade more than 90% various organics within 40 min under simulated sunlight illumination. The advantages of DEPFC treating organic-containing radioactive wastewater are: (1) the rear-mounted SC provides greater interior drivingpowers than conventional PFCs, resulting in a more efficiently charge separation; (2) the presence of ZrO_2 and O in porous carbon structure increases the wettability of ZrON-C/CF cathode, and thereby promoting the UO_2^{2+} adsorption; (3) the introduction of ZrO_2 induces the electrons transfer from ZrO_2 to N sites due to the high work function; (4) N-doping improves the adsorption efficiency of ZrON-C/CF cathode to UO_2^{2+} owing to enhanced electronegativity and increased varieties of nitrogen-containing functional groups. Overall, this work can present efficient technologies for simultaneously recycling uranium and degrading organics from complicated radioactive wastewater/polluted waters, and also provides new views in designing high-efficiency uranium reduction cathode materials.

CRediT authorship contribution statement

Zeng Qingming: Data curation, Formal analysis. **Zhang Qingsong:** Conceptualization, Data curation, Formal analysis, Funding acquisition, Writing – original draft, Writing – review & editing. **Zeng Qingyi:** Conceptualization, Funding acquisition, Project administration, Resources, Writing – review & editing. **Gong Haiyi:** Data curation, Formal analysis. **Zhang YaoYao:** Data curation, Formal analysis. **Zhang Qingyan:** Data curation, Formal analysis. **Deng Qimou:** Data curation, Formal analysis, Writing – original draft. **Zhang Chunlei:** Data curation, Formal analysis. **Xiao Yang:** Conceptualization, Formal analysis, Writing – original draft.

Declaration of Competing Interest

The authors declare that they have no known competing financial interests or personal relationships that could have appeared to influence the work reported in this paper.

Data Availability

Data will be made available on request.

Acknowledgments

This work was supported by the National Natural Science Foundation of China (12305387, 52170083), the Hunan Provincial Natural Science Foundation of China (2022JJ40376, 2021JJ20007), the Research Foundation of Education Bureau of Hunan Province, China (21B0441), the Science and Technology Innovation Program of Hunan Province (2022RC1125). The authors would like to thank Shiyanjia Lab (www.shiyanjia.com) for the support of DFT calculation. The comments and advice from editor and anonymous reviewers are highly appreciated, which help greatly enhance the overall quality of the paper.

Appendix A. Supporting information

Supplementary data associated with this article can be found in the online version at doi:10.1016/j.apcatb.2024.123808.

References

[1] X.J. Liu, F. Gao, T.T. Jin, K. Ma, H.J. Shi, M. Wang, Y.N. Gao, W.J. Xue, J. Zhao, S. T. Xiao, Y.G. Ouyang, G.A. Ye, Efficient and selective capture of thorium ions by a covalent organic framework, Nat. Commun. 14 (2023) 5097.
[2]] M. Mirza, R. Abdulaziz, W.C. Maskell, S. Wilcock, A.H. Jones, S. Woodall, A. Jackson, P.R. Shearing, D.J.L. Brett, Electrochemical processing in molten salts-a nuclear perspective, Energy Environ. Sci. 16 (2023) 952–982.
[3] R. Leng, Y.C. Sun, C.Z. Wang, Z. Qu, R. Feng, G.X. Zhao, B. Han, J.J. Wang, Z.Y. Ji, X.K. Wang, Design and fabrication of hypercrosslinked covalent organic adsorbents for selective uranium extraction, Environ. Sci. Technol. 57 (2023) 9615–9626.
[4] W.H. Lu, M.Y. Xu, F.L. Chen, P. Liu, D.B. Hua, Polyphosphonate-segmented macroporous organosilicon frameworks for efficient dynamic enrichment of uranium with in-situ regeneration, J. Hazard. Mater. 458 (2023) 131912.
[5] Y. Zhou, J.Q. Yang, N.Y. Zhou, H.X. Hao, X. Jiang, F. Lei, K.L. Shi, Y.H. Zhao, G. Zhou, T.H. Liu, S. Xing, Amidoxime-Functionalized MXene beads for the effective capture of uranium from wastewater with high fluoride concentrations, Chem. Eng. J. 471 (2023) 144647.
[6] Z. Wang, L.Y. Zhang, Z. Lei, L.Y. Zheng, L.Q. Huang, S. Liu, Y.X. Lu, Carbon dots and polyurethane composite for photo-induced elimination of uranium under air atmosphere, Chin. Chem. Lett. 34 (2023) 108146.
[7] Y.Q. Wu, K. Liu, Y.R. Chen, W. Xu, S.H. Zeng, W.R. Cui, Redox-active conjugated microporous polymer with favourable six-membered chelate ring for enhanced uranium extraction from highly acidic environments, Sep. Purif. Technol. 322 (2023) 124383.
[8] H.H. Wang, H. Guo, N. Zhang, Z.S. Chen, B.W. Hu, X.K. Wang, Enhanced photoreduction of U(VI) on C_3N_4 by Cr(VI) and BisphenolA: ESR, XPS, and EXAFS investigation, Environ. Sci. Technol. 53 (2019) 6454–6461.
[9] J. Duan, H.D. Jia, T.Y. Xu, F. Pan, X.N. Liu, W. Liu, D.Y. Zhao, Simultaneous adsorption of uranium(VI) and 2-chlorophenol by activated carbon fiber supported/modified titanate nanotubes (TNTs/ACF): Effectiveness and synergistic effects, Chem. Eng. J. 406 (2021) 126752.
[10] C.A. Velasco, A.J. Brearley, J. Gonzalez-Estrella, A.M.S. Ali, M.I. Meza, S. E. Cabaniss, B.M. Thomson, T.Z. Forbes, J.S.L. Pacheco, J.M. Cerrato, From adsorption to precipitation of U(VI): What is the role of pH and natural organic matter? Environ. Sci. Technol. 55 (2021) 16246–16256.

[11] N. Liu, J. Yu, H.S. Zhang, J.H. Zhu, Q. Liu, R.R. Chen, Y. Li, R.M. Li, J. Wang, Fe-MMT/WO_3 composites for chemical and photocatalysis synergistic reduction of uranium (VI), Chemosphere 344 (2023) 140321.
[12] P. Li, N.A. Vermeulen, X.R. Gong, C.D. Malliakas, J.F. Stoddart, J.T. Hupp, O. K. Farha, Design and synthesis of a water-stable anionic uranium-based metal–organic framework (MOF) with ultra large pores, Angew. Chem. Int. Ed. 55 (2016) 10358–10362.
[13] L. Yang, H. Xiao, Y. Qian, X. Zhao, X.-Y. Kong, P. Liu, W. Xin, Fu Lin, L. Jiang, L. Wen, Bioinspired hierarchical porous membrane for efficient uranium extraction from seawater, Nat. Sustain. 5 (2022) 71–80.
[14] E. Gkika, A. Troupis, A. Hiskia, E. Papaconstantinou, Photocatalytic reduction of chromium and oxidation of organics by polyoxometalates, Appl. Catal. B- Environ. 62 (2006) 28–34.
[15] Z.M. Dong, C. Meng, Z.F. Li, D.L. Zeng, Y.C. Wang, Z.P. Cheng, X.H. Cao, Q. Ren, Y. Q. Wang, X.Y. Li, Z.B. Zhang, Y.H. Liu, Novel Co_3O_4@TiO_2@CdS@Au double-shelled nanocage for high-efficient photocatalysis removal of U(VI): Roles of spatial charges separation and photothermal effect, J. Hazard. Mater. 452 (2023) 131248.
[16] C.H. Zhou, J.H. Li, J.C. Wang, C.Y. Xie, Y. Zhang, L. Li, T.S. Zhou, J. Bai, H. Zhu, B. X. Zhou, Efficient H_2 production and TN removal for urine disposal using a novel photoelectrocatalytic system of Co_3O_4/$BiVO_4$-MoNiCuO_x/Cu, Appl. Catal. B-Environ. 324 (2023) 122229.
[17] C.Y. Wang, Y.X. Liu, R. Chen, X. Zhu, D.D. Ye, Y. Yang, Q. Liao, Gas diffusion TiO_2 photoanode for photocatalytic fuel cell towards simultaneous VOCs degradation and electricity generation, J. Hazard. Mater. 447 (2023) 130769.
[18] J.H. Li, X.C. Li, S.B. Yu, S. Gao, Y. Zhang, Y. Li, C.Z. Wang, Q. Wang, Photocatalytic fuel cell for simultaneous antibiotic wastewater treatment and electricity production by anatase TiO_2 nanoparticles anchored on Ni foam, Chin. Chem. Lett. 34 (2023) 107417.
[19] T.S. Zhou, S. Chen, L.S. Li, J.C. Wang, Y. Zhang, J.H. Li, J. Bai, L.G. Xia, Q.J. Xu, M. Rahim, B.X. Zhou, Carbon quantum dots modified anatase/rutile TiO_2 photoanode with dramatically enhanced photoelectrochemical performance, Appl. Catal. B-Environ. 269 (2020) 118776.
[20] S.L. He, D.X. Xie, B.L. Wang, M.S. Zhu, S.J. Hu, Photocatalytic fuel cell based on integrated silicon nanowire arrays/zinc oxide heterojunction anode for simultaneous wastewater treatment and electricity production, J. Colloid Interf. Sci. 650 (2023) 1993–2002.
[21] Q. Sun, B. Han, K.J. Li, L.Y. Yu, L.F. Dong, The synergetic degradation of organic pollutants and removal of Cr(VI) in a multifunctional dual-chamber photocatalytic fuel cell with Ag@Fe_2O_3 cathode, Sep. Purif. Technol. 281 (2022) 119966.
[22] S.M. Lam, J.C. Sin, H.H. Zeng, H. Lin, H.X. Li, Z.Z. Qin, J.W. Lim, A.R. Mohamed, Z-scheme MoO_3 anchored-hexagonal rod like ZnO/Zn photoanode for effective wastewater treatment, copper reduction accompanied with electricity production in sunlight-powered photocatalytic fuel cell, Sep. Purif. Technol. 265 (2021) 118495.
[23] M. Deng, J. Ma, C. Yang, T. Cao, M. Yao, F. Liu, H. Chen, X. Wang, Facile construction of a highly dispersed PdCo nanocatalyst supported on NH_2-UiO-66-derived N/O co-doped carbon for hydrogen evolution from formic acid, Mater. Today Chem. 24 (2022) 101001.
[24] S.B. Wang, Y. Wang, S.L. Zhang, S.Q. Zang, X. W. (D.) Lou, Supporting ultrathin $ZnIn_2S_4$ nanosheets on Co/N-doped graphitic carbon nanocages for efficient photocatalytic H_2 generation, Adv. Mater. 31 (2019) 1903404.
[25] L. Lyu, D.B. Yan, G.F. Yu, W.R. Cao, C. Hu, Efficient destruction of pollutants in water by a dual-reaction center Fenton-like process over carbon nitride compounds complexed Cu(II)-$CuAlO_2$, Environ. Sci. Technol. 52 (2018) 4294–4304.
[26] F.C. Zheng, Y. Yang, Q.W. Chen, High lithium anodic performance of highly nitrogen-doped porous carbon prepared from a metal-organic framework, Nat. Commun. 5 (2014) 5261.
[27] K.P. Gong, F. Du, Z.H. Xia, M. Durstock, L.M. Dai, Nitrogen-Doped carbon nanotube arrays with high electrocatalytic activity for oxygen reduction, Science 323 (2009) 760–764.
[28] Z.M. Lv, J. Zhang, Y.F. Zhang, K.X. Li, X.S. Ye, M. Fang, X.L. Tan, M.G. Kong, X. K. Wang, Selective and efficient removal of radioactive ions from water with well-dispersed metal oxide nanoparticles@N-doped carbon, Sep. Purif. Technol. 285 (2022) 120366.
[29] D.T. Oyekunle, B.B. Wu, F. Luo, J. Ali, Z.Q. Chen, Synergistic effects of Co and N doped on graphitic carbon as an in situ surface-bound radical generation for the rapid degradation of emerging contaminants, Chem. Eng. J. 421 (2021) 129818.
[30] B.B. Yin, R. Liang, X.X. Liang, D. Fu, L. Wang, G.X. Sun, Construction of stable wide-temperature-range proton exchange membranes by incorporating a carbonized metal–organic frame into polybenzimidazoles and polyacrylamide hydrogels, Small 17 (2021) 2103214.
[31] B. Chi, L.H. Zhang, X.X. Yang, Y.C. Zeng, Y.J. Deng, M.R. Liu, J.L. Huo, C.Z. Li, X. R. Zhang, X.D. Shi, Y.J. Shao, L. Gu, L.R. Zheng, Z.M. Cui, S.J. Liao, G. Wu, Promoting ZIF-8-derived Fe-N-C oxygen reduction catalysts via Zr doping in proton exchange membrane fuel cells: Durability and activity enhancements, ACS Catal. 13 (2023) 4221–4230.
[32] S. Chang, C. Hu, A. Beyhaqi, M.Q. Wang, Q.Y. Zeng, Highly efficient hydrogen and electricity production combined with degradation of organics based on a novel solar water-energy nexus system, ACS Appl. Mater. Interfaces 12 (2020) 2505–2515.
[33] W.Q. Wang, L. Wang, Y. Li, S. Liu, Z.G. Xie, X.B. Jing, Nanoscale polymer metal-organic framework hybrids for effective photothermal therapy of colon cancers, Adv. Mater. 28 (2016).
[34] W. Cao, Y. Zhang, Z. Shi, T. Liu, X.S. Song, L.S. Zhang, P.K. Wong, Z.G. Chen, Boosting the adsorption and photocatalytic activity of carbon fiber/MoS_2-based weavable photocatalyst by decorating UiO-66-NH_2 nanoparticles, Chem. Eng. J. 417 (2021) 128112.
[35] J.M. Huang, P. Xue, S. Wang, S.J. Han, L.G. Lin, X. Chen, Z.B. Wang, Fabrication of zirconium-based metal-organic frameworks@tungsten trioxide (UiO-66-NH_2@WO_3) heterostructure on carbon cloth for efficient photocatalytic removal of tetracycline antibiotic under visible light, J. Colloid Interf. Sci. 606 (2022) 1509–1523.
[36] M. Golpour, M. Pakizeh, Preparation and characterization of new PA-MOF/PPSU-GO membrane for the separation of KHI from water, Chem. Eng. J. 345 (2018) 221–232.
[37] P.D. Wu, H. Li, Z. Fang, Synergistic Catalysis of Co-Zr/CNx Bimetallic nanoparticles enables reductive amination of biobased levulinic acid, Adv. Sustain. Syst. 6 (2022) 2100321.
[38] X.L. Guo, J.H. Duan, C.J. Li, Z.S. Zhang, W.W. Wang, Fabrication of highly stabilized Zr Doped g-C_3N_4/Nb_2O_5 heterojunction and its enhanced photocatalytic performance for pollutants degradation under visible light irradiation, Colloid Surf. A 649 (2022) 129474.
[39] M. Wang, Z.Z. Yang, W.H. Li, L. Gu, Y. Yu, Superior sodium storage in 3D interconnected nitrogen and oxygen dual-doped carbon network, Small 12 (2016) 2559–2566.
[40] S. Li, J.X. Qiu, C. Lai, M. Ling, H.J. Zhao, S.Q. Zhang, Surface capacitive contributions: towards high rate anode materials for sodium ion batteries, Nano Energy 12 (2015) 224–230.
[41] C.Q. Yuan, X.H. Liu, M.Y. Jia, Z.X. Luo, J.N. Yao, Facile preparation of N- and O-doped hollow carbon spheres derived from poly(ophenylenediamine) for supercapacitors, J. Mater. Chem. A 3 (2015) 3409.
[42] L. Sun, C.G. Tian, Y. Fu, Y. Yang, J. Yin, L. Wang, H.G. Fu, Nitrogen-Doped porous graphitic carbon as an excellent electrode material for advanced supercapacitors, Chem. Eur. J. 20 (2014) 564–574.
[43] C.V. Reddy, A. Nagar, N.P. Shetti, I.N. Reddy, S. Basu, J. Shim, R.R. Kakarla, Novel g-C_3N_4/$BiVO_4$ heterostructured nanohybrids for high efficiency photocatalytic degradation of toxic chemical pollutants, Chemosphere 322 (2023) 138146.
[44] P.L. Liang, L.Y. Yuan, K. Du, L. Wang, Z.J. Li, H. Deng, X.C. Wang, S.Z. Luo, W. Q. Shi, Photocatalytic reduction of uranium(VI) under visible light with 2D/1D Ti_3C_2/CdS, Chem. Eng. J. 420 (2021) 129831.
[45] Z.B. Zhang, Z.F. Li, Z.M. Dong, F.T. Yu, Y.C. Wang, Y.Q. Wang, X.H. Cao, Y.H. Liu, Y.H. Liu, Synergy of photocatalytic reduction and adsorption for boosting uranium removal with PMo_{12}/UiO-66 heterojunction, Chin. Chem. Lett. 33 (2022) 3577–3580.
[46] Y. Xie, C.L. Chen, X.M. Ren, X.X. Wang, H.Y. Wang, X.K. Wang, Emerging natural and tailored materials for uranium-contaminated water treatment and environmental remediation, Prog. Mater. Sci. 103 (2019) 180–234.
[47] V.N. Salomone, J.M. Meichtry, G. Zampieri, M.I. Litter, New insights in the heterogeneous photocatalytic removal of U(VI) in aqueous solution in the presence of 2-propanol, Chem. Eng. J. 261 (2015) 27–35.
[48] X.F. Li, Y.L. Qiu, Z.L. Zhu, T. Chen, H. Zhang, D.Q. Yin, Construction of magnetically separable dual Z-scheme g-C_3N_4/α-Fe_2O_3/Bi_3TaO_7 photocatalyst for effective degradation of ciprofloxacin under visible light, Chem. Eng. J. 440 (2022) 135840.
[49] B. Wang, X.X. Zhang, L.C. Li, M.T. Ji, Z. Zheng, C.H. Shi, Z. Li, H. Hao, A complete method for evaluating the performance of photocatalysts for the degradation of antibiotics in environmental remediation, J. Vis. Exp. (188) (2022) e64478.
[50] K.F. Yu, L. Tang, X. Cao, Z.H. Guo, Y. Zhang, N. Li, C.X. Dong, X. Gong, T. Chen, R. He, W.K. Zhu, Semiconducting metal-organic frameworks decorated with spatially separated dual cocatalysts for efficient uranium(VI) photoreduction, Adv. Funct. Mater. 20 (2022) 2200315.
[51] X. Li, S.W. Wang, P. Chen, B.K. Xu, X. Zhang, Y.H. Xu, R. Zhou, Y. Yu, H.L. Zheng, P. Yu, Y.J. Sun, ZIF-derived non-bonding Co/Zn coordinated hollow carbon nitride for enhanced removal of antibiotic contaminants by peroxymonosulfate activation: Performance and mechanism, Appl. Catal. B-Environ. 325 (2023) 122401.
[52] X.H. Jiang, Q.J. Xing, X.B. Luo, F. Li, J.P. Zou, S.S. Liu, X. Li, X.K. Wang, Simultaneous photoreduction of Uranium(VI) and photooxidation of Arsenic(III) in aqueous solution over g-C_3N_4/TiO_2 heterostructured catalysts under simulated sunlight irradiation, Appl. Catal. B-Environ. 228 (2018) 29–38.
[53] Y.F. Zhang, M.Y. Zhu, S. Zhang, Y.W. Cai, Z.M. Lv, M. Fang, X.L. Tan, X.K. Wang, Highly efficient removal of U(VI) by the photoreduction of SnO_2/$CdCO_3$/CdS nanocomposite under visible light irradiation, Appl. Catal. B-Environ. 279 (2020) 119390.
[54] T.M. Budnyak, A. Gładysz-Płaska, A.V. Strizhak, D. Sternik, I.V. Komarov, M. Majdan, V.A. Tertykh, Imidazole-2yl-Phosphonic acid derivative grafted onto mesoporous silica surface as a novel highly effective sorbent for uranium(VI) ion extraction, ACS Appl. Mater. Interfaces 10 (2018) 6681–6693.
[55] B. Zhang, X. He, C.Z. Yu, G.C. Liu, D. Ma, C.Y. Cui, Q.H. Yan, Y.J. Zhang, Gu. S. Zhang, J. Ma, Y.J. Xin, Degradation of tetracycline hydrochloride by ultrafine TiO_2 nanoparticles modified g-C_3N_4 heterojunction photocatalyst: Influencing factors, products and mechanism insight, Chin. Chem. Lett. 33 (2022) 1337–1342.
[56] W.C. Xu, S.F. Lai, S.C. Pillai, W. Chu, Y. Hu, X.D. Jiang, M.L. Fu, X.L. Wu, F.H. Li, H.L. Wang, Visible light photocatalytic degradation of tetracycline with porous Ag/graphite carbon nitride plasmonic composite: degradation pathways and mechanism, J. Colloid Interface Sci. 574 (2020) 110–121.
[57] J. Liao, T. Xiong, L. Ding, Y. Xie, Y. Zhang, W.K. Zhu, Design of a renewable hydroxyapatite biocarbon composite for the removal of uranium(VI) with high efficiency adsorption performance, Biochar 4 (2022) 29.
[58] B. Tansel, Significance of thermodynamic and physical characteristics on permeation of ions during membrane separation: Hydrated radius, hydration free energy and viscous effects, Sep. Purif. Technol. 86 (2012) 119–126.

[59] L. Wang, X. Huang, M.E. Han, L. Lyu, T. Li, Y.W. Gao, Q.Y. Zeng, C. Hu, Efficient inhibition of photogenerated electron-hole recombination through persulfate activation and dual-pathway degradation of micropollutants over iron molybdate, Appl. Catal. B-Environ. 257 (2019) 117904.
[60] M.J. Hao, Y.H. Xie, X.L. Liu, Z.S. Chen, H. Yang, G.I.N. Waterhouse, S.Q. Ma, X. K. Wang, Modulating uranium extraction performance of multivariate covalent organic frameworks through donor−acceptor linkers and amidoxime nanotraps, JACS Au 3 (2023) 239–251.
[61] X. Wang, M.H. Lou, X.T. Yuan, W.J. Dong, C.L. Dong, H. Bi, F.Q. Huang, Nitrogen and oxygen dual-doped carbon nanohorn for electrochemical capacitors, Carbon 118 (2017) 511–516.
[62] H. Liu, S.H. Cao, L. Chen, K. Zhao, C.B. Wang, M.X. Li, S.G. Shen, W.J. Wang, L. Ge, Electron acceptor design for 2D/2D iodinene/carbon nitride heterojunction boosting charge transfer and CO_2 photoreduction, Chem. Eng. J. 433 (2022) 133594.
[63] W. Wang, Q. Luo, L.Q. Li, Y.F. Wang, X.B. Huo, S.P. Chen, X.W. Du, N. Wang, Ni-Single-Atom mediated 2D heterostructures for highly efficient uranyl photoreduction, Adv. Funct. Mater. (2023) 2302913.
[64] L. Hao, R.C. Shen, C. Huang, Z.Z. Liang, N. Li, P. Zhang, X.Z. Li, C.C. Qin, X. Li, Fluorenone-based covalent organic frameworks with efficient exciton dissociation and well-defined active center for remarkable photocatalytic hydrogen evolution, Appl. Catal. B-Environ. 330 (2023) 122581.
[65] C. Wang, H. Jiao, Y.B. Yang, Y.C. Wu, P. Na, Dual-Functional S-Scheme Fe_3O_4/TiO_2/g-C_3N_4 double-heterostructure bridged by TiO_2 for collaborative removal of U(VI) and Sb(III,), J. Clean. Prod. 426 (2023) 139114.
[66] D.D. Gao, W. Zhong, X.D. Zhang, P. Wang, H.G. Yu, Free-electron inversive modulation to charge antibonding orbital of ReS_2 cocatalyst for efficient photocatalytic hydrogen generation, Small 09123 (2023).
[67] B.Y. Tu, K.F. Yu, D.J. Fu, L. Zhou, R.X. Wang, X.Y. Jiang, H.H. Liu, X. Cao, X. Gong, R. He, Y.J. Tang, T. Chen, W.K. Zhu, Amino-rich Ag-NWs/NH_2-MIL-125(Ti) hybrid heterostructure via LSPR effect for photo-assist uranium extraction from fluorine-containing uranium wastewater without sacrificial agents, Appl. Catal. B-Environ. 337 (2023) 122965.